Characterization of glass fiber reinforced polymer via Digital Volume Correlation: Investigation of notch sensitivity

Ana Vrgoč, Zvonimir Tomičević, Benjamin Smaniotto, François Hild

To cite this version:

Ana Vrgoč, Zvonimir Tomičević, Benjamin Smaniotto, François Hild. Characterization of glass fiber reinforced polymer via Digital Volume Correlation: Investigation of notch sensitivity. Mechanics of Materials, 2023, 177 (9), pp.104552. 10.1016/j.mechmat.2022.104552 . hal-03916417

HAL Id: hal-03916417
https://hal.science/hal-03916417v1

Submitted on 30 Dec 2022

Characterization of glass fiber reinforced polymer via Digital Volume Correlation: Investigation of notch sensitivity

Ana Vrgoč[a], Zvonimir Tomičević[a,], Benjamin Smaniotto[b], François Hild[b]

[a]University of Zagreb, Faculty of Mechanical Engineering and Naval Architecture
Ivana Lučića 5, 10002 Zagreb, Croatia
[b]Université Paris-Saclay, CentraleSupélec, ENS Paris-Saclay, CNRS
LMPS - Laboratoire de Mécanique Paris-Saclay, 91190 Gif-sur-Yvette, France

---

Abstract

The results of *in-situ* cyclic tensile experiments performed on two dogbone specimens made of glass fiber mat reinforced polyester resin are presented (the second specimen contains a machined rectangular notch). The experimental data were obtained by using X-Ray Computed Tomography. The reconstructed volumes were analyzed via Digital Volume Correlation. The investigated material was notch-insensitive since both specimens failed at equal stress levels. To further confirm this hypothesis, and to study strain-damage interactions, the major eigen strain and correlation residual maps of both specimens were analyzed. Even in the first loading cycle, an inner strained band extending through the whole ligament area developed within both specimens, already indicating the path to final fracture. It is shown that the final failure of the studied material was primarily driven by the yarn mesostructure, *i.e.*, the influence of the underlying heterogeneities prevailed over the effects due to specimen machining and/or geometric singularity.

Keywords: Polymer matrix composite, Digital Volume Correlation, Notch-sensitivity, Correlation residuals

---

[*]Corresponding author
Email address: `zvonimir.tomicevic@fsb.hr` (Zvonimir Tomičević)

1. Introduction

Fiber reinforced polymers (FRPs) are being increasingly used in major structural applications thanks to their advanced properties (*e.g.*, high stiffness-to-weight ratio, good formability during manufacturing) compared to conventional engineering materials [1, 2]. Notches, cut-outs and other types of geometric discontinuities are common features in industrial applications of FRP structures, as they *e.g.* facilitate joining of structural parts. Such geometric singularities induce undesirable strain and stress concentrations, which may lead to premature failure. Due to their heterogeneous nature, the mechanical response as well as the failure of FRPs, is a direct consequence of a cascade of events occurring at microstructural levels [3]. Hence, understanding the link between the heterogeneous mesostructure and final failure, especially in the presence of geometric discontinuities, is crucial for reliable prediction of FRP behavior during in-service life, as well as mitigating stress and strain concentration effects.

Extensive experimental analyses on notched FRP specimens under various loading regimes have shown that in the close vicinity of a notch root various damage mechanisms are induced due to high stress and strain gradients [1, 4, 5]. Yet, in the majority of available studies, the bulk kinematics was not measured *in-situ*, nor was it related to micro- and mesostructural features. A way to bridge this gap is coupling *in-situ* or *ex-situ* X-Ray Computed Tomography (XCT) mechanical tests with Digital Volume Correlation (DVC). The former is a non-destructive testing (NDT) method enabling for the visualization of microstructural changes in the material bulk during experiments. This imaging technique has given great impetus to experimental solid mechanics [6, 7]. As the use of FRPs has been reshaping various industrial branches (*e.g.*, automotive, aerospace, marine, power industries) [2], XCT has being increasingly employed to characterize damage phenomena in such materials. Coupling XCT and DVC into a unique framework enables for full-field displacement measurements and calculation of strain maps in the 3D space. Being the volumetric extension of the widely employed Digital Image Correlation (DIC) technique [8, 9, 10], DVC aims at measuring the deformation of investigated materials by correlating 3D images acquired between two states [7, 11]. The majority of existing DVC measurements of FRPs were carried out by employing local DVC [12, 13, 14]. Such algorithms discretize the inspected Region of Interest (ROI) into smaller sub-volumes, yet the displacement continuity between adjacent sub-volumes is not ensured (*i.e.*, they are registered independently) [15, 16]. Conversely, global approaches based on finite element (FE) discretization and assuming continuity of displacement fields were introduced [17, 18]. The key advantage of such approaches is the availability of correlation residuals corresponding to the gray level difference between the reference volume and the volume of the deformed material corrected by the measured displacement field [7]. Correlation residuals not only provide useful information on the convergence of DVC algorithms, but also unveil discontinuities (*i.e.*, damaged zones) for converged displacement fields [7, 19].

In this work, the results of *in-situ* cyclic tensile experiments performed on two dogbone specimens are presented; the second specimen contained a machined rectangular notch. The material studied herein is a continuous glass fiber mat reinforced polyester resin. The experiments were imaged via XCT and coupled with DVC to measure the bulk kinematics. Prior to analyzing the results of volumetric correlations, the measurement uncertainty levels of both experiments were quantified by correlating two scans of the undeformed configuration. The global material response of both experiments was characterized by virtual gauges positioned over the inspected ROIs. As both specimens failed at equal stress levels, it is concluded that the investigated material is notch-insensitive. To further confirm this hypothesis, major eigen strain fields were analyzed to study the strained band activity. The correlation residual maps were investigated to monitor damage onset and growth, as well as strain-damage interactions. Last, major eigen strain fields were laid over the corresponding reference mesostructure of different sections to study the effect of heterogeneous yarn mesostructure on the strained band development.

2. Material and methods

This section deals with the material and methods employed in the present study. First, the properties and fabrication procedure of the investigated material are introduced. Next, the basic principles of regularized FE-based DVC are summarized.

2.1. *Glass fiber reinforced polyester resin*

The investigated dogbone specimens were cut from a continuous glass fiber mat reinforced polyester resin composite plate. The latter was produced by manual lay-up followed by compression molding. The laminate comprised 12 plies of R-glass fiber mat laid in a polyester resin mixture. The laminate was cured under pressure for 24 h at room temperature, while post-curing was conducted at 100°C for 3h. The fiber volume fraction was found to be 40%, while that of the matrix was 55%. As vacuum was not applied during molding, the micrograph of the investigated material (Fig. 1) revealed the presence of air voids, the volume fraction of which was found to be 5%.

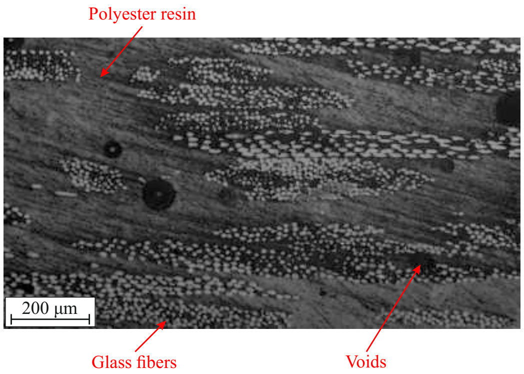

Fig 1. Optical micrograph of the glass fiber mat reinforced polyester resin composite studied herein.

2.2. *Global Digital Volume Correlation*

Digital Volume Correlation is a full-field measurement technique that enables for 3D displacement measurements not only on the surface, but in the bulk of investigated materials [7, 20, 11]. This technique consists in the registration of a 3D image $f(\mathbf{x})$ of the reference state (were $\mathbf{x}$ denotes the voxel location) and a series of images $g(\mathbf{x})$ of deformed configurations. The 3D images (*i.e.*, reconstructed volumes) are represented by a discrete gray level field (8-bit deep) of the voxel coordinate $\mathbf{x}$. Thus, each voxel inside the reconstructed volume carries the information on the material ability to absorb X-rays. The basic principle of DVC relies on matching the gray levels in the reference volume f (which is usually that of the undeformed state) and those of the deformed volume g. The gray level conservation is thus assumed to correlate the two reconstructed volumes

$$f(\mathbf{x}) = g(\mathbf{x} + \mathbf{u}(\mathbf{x})), \tag{1}$$

where $\mathbf{u}$ is the measured displacement field. However, the strict conservation of gray levels cannot be satisfied in real applications as the tomographic technique causes deviations due to its associated artifacts (*e.g.*, image noise, displacement discretizations, ring artifacts, spurious motions during scanning [7]). Consequently, the solution consists in minimizing the L2-norm of gray level residual $\varphi_c(\mathbf{x}) = f(\mathbf{x}) - g(\mathbf{x} + \mathbf{u}(\mathbf{x}))$ with respect to the kinematic unknowns related to the parameterization of the sought displacement amplitudes [21]

$$\Phi_c^2 = \sum_{\text{ROI}} \varphi_c^2(\mathbf{x}). \tag{2}$$

As a global (*i.e.*, FE-based) approach was employed in the present work, the global residual (Eq. (2)) is minimized with respect to the displacement field parameterized by using a kinematic basis comprising shape functions $\mathbf{\Psi}_n$ and nodal displacements u_n

$$\mathbf{u}(\mathbf{x}) = \sum_{n} u_n \mathbf{\Psi}_n(\mathbf{x}). \tag{3}$$

When the displacement field is parameterized as in Eq. (3), it is regularized with a continuity requirement *a priori* assumed for the kinematic solution. Additional mechanical knowledge may be implemented to enhance convergence of the algorithm, which is referred to as mechanical regularization based on the equilibrium gap method [19, 22, 23]. Such an approach enforces the smoothness of measured fields by acting as a low-pass filter that dampens out high spatial frequencies. This is achieved by tuning characteristic regularization lengths. Thus, when a FE discretization is employed, mechanical regularization is activated for any length greater than the characteristic element length.

One of the key advantages of global DVC is the availability of correlation residual maps φ_c for each analyzed volume. These residuals are probed for all voxels belonging to the studied ROI, and serve as a tool for correlation quality inspection (*e.g.*, when checking the convergence of DVC analysis). Due to the fact that damage growth impairs gray level conservation and consequently DVC convergence, the correlation residuals also provide the means for detecting damage initiation and monitoring damage growth [11, 19, 24, 25].

3. *In-situ* mechanical experiments

The present section addresses the experimental protocols employed herein. First, the specimen geometries are introduced. Both specimens were subjected to *in-situ* cyclic tensile loading. Next, the scanning parameters employed in both experimental configurations are outlined, followed by the description of the imaging and mechanical setup. Last, the loading and acquisition histories of the performed *in-situ* experiments are reported.

3.1. Unnotched dogbone specimen

The 5.2 mm thick unnotched specimen geometry is presented in Fig. 2(a). The dogbone geometry (*i.e.*, thinned central ligament) was selected to enforce specimen failure in the ligament area and not in the grips. The width of the narrowest gauge section was equal to 5.6 mm. The studied specimen was subjected to cyclic tension with the *in-situ* TTC Deben testing machine in the X50+ scanner (North Star Imaging) of LMPS. The experimental setup is shown in Fig. 2(b). The prescribed stroke-rate was 4 µm/s. The test consisted of 2 loading cycles corresponding to 35% and 70% of the specimen failure strength (σ_m = 135

MPa), as reported in Fig. 2(c). During the proposed experimental protocol, 6 scans in total were acquired in loaded and unloaded configurations (*i.e.*, after applying each loading step). The measured uniaxial force history revealed relaxation phenomena, yet limited, when holding the specimen at the high load levels of the prescribed loading cycles to acquire the radiographs (the force drop was approximately 160 N). No significant blur was observed on the reconstructed volumes.

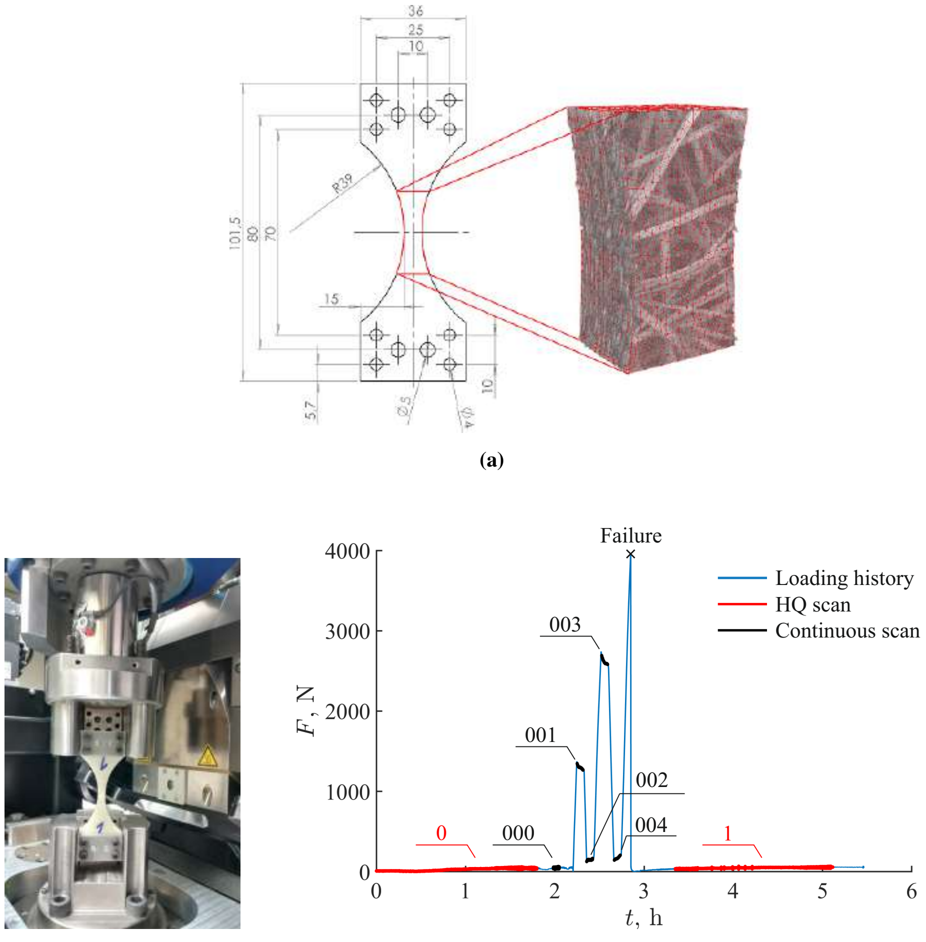

(a)

(b)

(c)

Fig 2. (a) Geometry of the investigated unnotched dogbone specimen together with the region of interest (depicted with red contour) and finite element mesh employed in DVC analyses. The size of the inspected region of interest was 875×553×1249 voxels, while the physical length of one voxel was equal to 14.6 µm. The average element length was equal to 14 voxels. (b) Deben testing machine inside the X50+ scanner (North Star Imaging) of LMPS. (c) Loading and acquisition history of the *in-situ* tensile test. The first scan was acquired in the unloaded state and was considered as the reference to evaluate measurement uncertainties and run correlations. Then, five additional scans were acquired for the purposes of bulk kinematic measurements. Last, a second HQ scan was performed *post-mortem*.

The first scan (0) corresponds to the unloaded state, and it was acquired with high quality (HQ) parameters (Table 1). As it resulted in low noise levels, this acquisition was considered as the reference to quantify measurement uncertainties and perform subsequent correlations. It enabled microstructural features to be imaged in more detail. However, the entire reference scan required approximately 2 h to be completed. To conduct the experiment in a reasonable time, the number of averaging frames for all subsequent acquisitions was switched to 1 (continuous scanning parameters), which led to 4 min acquisitions. In such a way, relaxation phenomena could be mitigated. For the continuous parameters, the projections were acquired continuously while the specimen was loaded and rotated. Moreover, 3D scans consisted of different numbers of radiographs (800 for HQ and 768 for continuous scanning parameters) captured at equally spaced angles ranging over a full 360° revolution. A filtered-back projection algorithm was employed to reconstruct 3D images from series of acquired radiographs [26], and no filtering was applied. The original size of the volumes encoded as 8-bit deep gray levels was $1507 \times 1507 \times 1849$ voxels. Since performing volumetric correlations with the full-size reconstructed volumes would be computationally too demanding, only a part of the reconstructed volume was considered herein. The size of the ROI tailored to the actual specimen geometry and focusing on the thinned ligament was $875\times553\times1249$ voxels (Fig. 2(a)). The physical size of one voxel was 14.6 μm.

Table 1. DVC hardware parameters.

Tomograph	North Star Imaging X50+	
X-ray source	XRayWorX XWT-240-CT	
Target/ Anode	W (reflection mode)	
Filter	None	
Voltage	145 kV	
Current	78 µA	
Focal spot size	5 µm	
Tube to detector	910 mm	
Tube to object	53 mm	
Detector	Dexela 2923	
Definition	1507 × 1849 pixels (2 × 2 binning)	
Scanning settings	High quality	Continuous
Number of projections	800	768
Angular amplitude	360°	360°
Frame average	20 per projection	Continuous (1 per step)
Frame rate	3 fps	3 fps
Acquisition duration	1 h 46 min 26 s	4 min 26 s
Reconstruction algorithm	Filtered back-projection	Filtered back-projection
Gray level amplitude	8 bits	8 bits
Field of view	$7.3 \times 10 \times 20.5$ mm^3	$7.3 \times 10 \times 20.5$ mm^3
Image scale	14.6 µm/voxel	14.6 µm/voxel

3.2. *Single notched dogbone specimen*

Another 5.2 mm thick dogbone specimen was considered in the present study. A rectangular notch was cut on the one side of the specimen narrowest gauge section to induce strain gradients (Fig. 3(a)). The notch depth was equal to 1.6 mm, while the width of the notch was 0.6 mm. The single notched specimen was subjected to *in-situ cyclic* tensile loading, and also imaged in the X50+ scanner with identical parameters as before (Table 1). The stroke velocity was equal to 4 µm/s, *i.e.*, the same as for the unnotched specimen. Four loading cycles corresponding to 25%, 50%, 75% and 90% of the failure strength were carried out (Fig. 3(b)). The choice of the load levels was based upon the first experiment (*i.e.*, the failure strength of the unnotched specimen). The measured uniaxial force history revealed rapid but limited relaxation (the drop of the peak force was approximately 160 N) during the acquisition of scans 001, 003 and 005. At the peak of the fourth loading cycle, fast relaxation was followed by a more gradual decrease. During the acquisition of scans 007 and 008, the observed force decrease was approximately 50 N. These relaxations did not significantly influence the reconstruction quality of the 3D images.

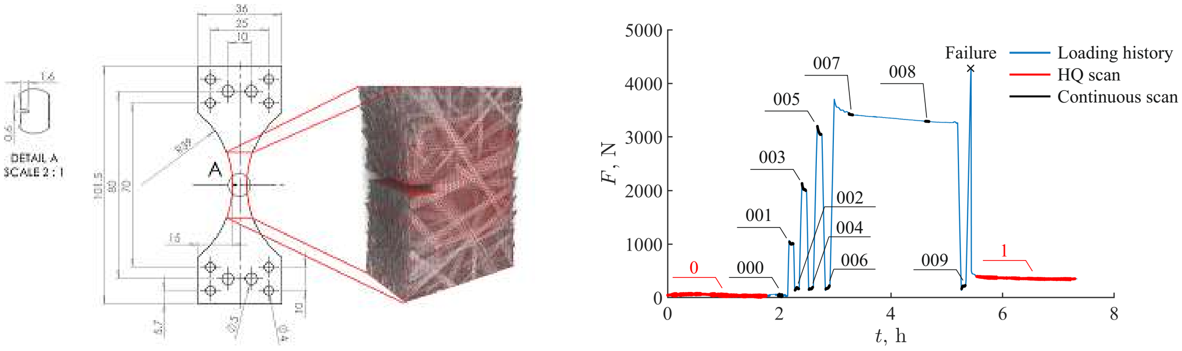

(a)

(b)

Fig 3. (a) Geometry of the investigated single notched dogbone specimen together with the region of interest (depicted with red contour) and finite element mesh employed in DVC analyses. The size of the inspected region of interest was 680×465×1001 voxels, while the physical length of one voxel was equal to 14.6 µm. The average element length was equal to 11 voxels. (b) Loading and acquisition history of the *in-situ* tensile test. The first scan was acquired in the unloaded state and was considered as the reference to evaluate measurement uncertainties and run correlations. Then, 10 additional scans were acquired for the purposes of *in-situ* bulk kinematic measurements. Last, a second HQ scan was performed *post-mortem*.

During the *in-situ* experiment of the single notched specimen, 11 scans in total were acquired in loaded/unloaded states. The same scanning parameters as for the unnotched specimen were employed, *i.e.*, HQ and continuous. The first HQ scan was acquired in the unloaded configuration (Fig. 3(a)). This acquisition was considered as the reference for the quantification of measurement uncertainties, as well as for subsequent correlation analyses. As for the unnotched specimen, the volumes were reconstructed employing a filtered-back projection algorithm [26], and no filtering was applied when reconstructing the 3D images. The size of the inspected ROI, tailored to the thinned ligament, was equal to 680×465×1001 voxels (Fig. 3(a)), while the physical size of one voxel was 14.6 μm.

4. Results

In this section, the results of DVC correlations are presented. The measurement uncertainty levels of both experiments were first evaluated by correlating the two scans of the unloaded configuration. Due to complex damage phenomena and fracture, correlation analyses were not performed on the *post-mortem* scans. Next, the mechanical characterization was performed to characterize the global material response of both experiments. As both specimens broke at the equal stress level, it was concluded that the investigated material is notch-insensitive. To further investigate this hypothesis, major eigen strain fields and correlation residual maps of both specimens were studied to analyze strained band activity, as well as to monitor damage initiation and growth.

4.1. Measurement uncertainty quantification

The volumes acquired during both *in-situ* cyclic tests were analyzed via regularized FE-based DVC implemented within the Correli 3.0 framework [27]. The inspected ROIs were discretized using first-order tetrahedral elements (T4) to properly describe the specimen boundaries. The FE meshes tailored to the actual specimen geometries are shown in Fig. 2(a) and Fig. 3(a). The average element length of the unnotched specimen, calculated as the cube root of the mean element volume, was 14 voxels, while that of the single notched specimen was 11 voxels. Such element lengths were chosen to properly capture the bulk kinematics, as well as high gradients in the investigated heterogeneous mesostructures. Moreover, as it was *a priori* assumed that the notch would induce high strain gradients and damage phenomena would concentrate in that area, the notched region was discretized with even smaller elements (8 voxels) than the remainder of the inspected ROI (14 voxels). However, fine FE meshes yield higher measurement uncertainties [7, 22]. Thus, mechanical regularization was employed to reduce the uncertainty levels, while maintaining the same spatial resolution.

The measurement uncertainties were evaluated in terms of standard deviations (Std) of measured displacements and calculated major eigen strain fields, as reported in Table 2. These quantities present the limits above which the mechanical signal is distinguished from noise. Let us emphasize that the reported levels were assessed by correlating scans 0 (HQ) and 000 (continuous) acquired prior to cycling the specimens. As the correlation technique relies on image contrast induced by the underlying mesostructure, the root mean squared (RMS) norm of the image gradient ($\boldsymbol{\nabla} f$) over the inspected ROIs is also reported in Table 2. Next, major eigen strain fields were computed from the measured displacement data. The strain uncertainty levels were calculated as the standard deviation of nodal values of major eigen strains extrapolated from the FE mesh. In general, low levels of contrast, *i.e.*, low image gradients, are more challenging for DVC analyses [7]. When comparing the values reported in Table 2, the single notched specimen yielded higher measurement uncertainties, even though the reported image gradient was higher than that of the unnotched specimen. This is due to the decreased spatial resolution (*i.e.*, the mesh was refined in the notched area). The reported displacement and strain uncertainty levels are related to the tomographic technique together with its intrinsic artifacts (*e.g.*, image noise, ring artifacts, displacement discretizations, spurious motions during scanning [7]). An additional source of uncertainty arose from the fact that scans of different qualities were correlated (*i.e.*, HQ scan 0 and continuous scan 000). The reported values are deemed low.

Table 2. Standard displacement and strain uncertainties of DVC measurements, as well as RMS norm of the image gradient.

	Unnotched	Single notched
Std(U_x)	0.03 vx	0.04 vx
Std(U_y)	0.02 vx	0.03 vx
Std(U_z)	0.02 vx	0.03 vx
Std(ε_1)	5.9×10^{-5}	8×10^{-4}
RMS(∇f)	17.1 GL/vx	21.8 GL/vx

4.2. Mechanical characterization

The global material response of both experiments was obtained with DVC virtual gauges positioned over the inspected ROIs. Then, the Young's modulus of both experiments was estimated based on experimental data and full-field measurements, *i.e.*, uniaxial stress calculated as the ratio of applied force by the initial cross-sectional area of specimen ligament and mean major eigen strains. Figure 4(a) shows the mean eigen strain history for the unnotched specimen. The mean major eigen strain level of 0.003 reported for scan 000 stems from measurement uncertainties. The elevated strain values were primarily reported for the surface nodes of the specimen ligament edges, and thus contributed to the mean major eigen strain level. This effect could be mitigated by employing higher regularization lengths for those nodes, which would yield even smoother fields. The prescribed load at the peak of the first loading cycle ($F = 1375$ N) resulted in a 0.008 mean major eigen strain. Based on these levels, the Young's modulus of the first loading cycle was estimated to be 9 GPa. Furthermore, a loss of stiffness during the subsequent loading cycle (between scans 002 and 003) was detected from the reported stress-strain response (the Young's modulus degraded by about 23%). Low permanent strains were observed in the last unloading stage prior to specimen failure (scan 004). In addition, the investigated unnotched specimen broke at $F = 3968$ N, which led to a failure strength equal to 135 MPa.

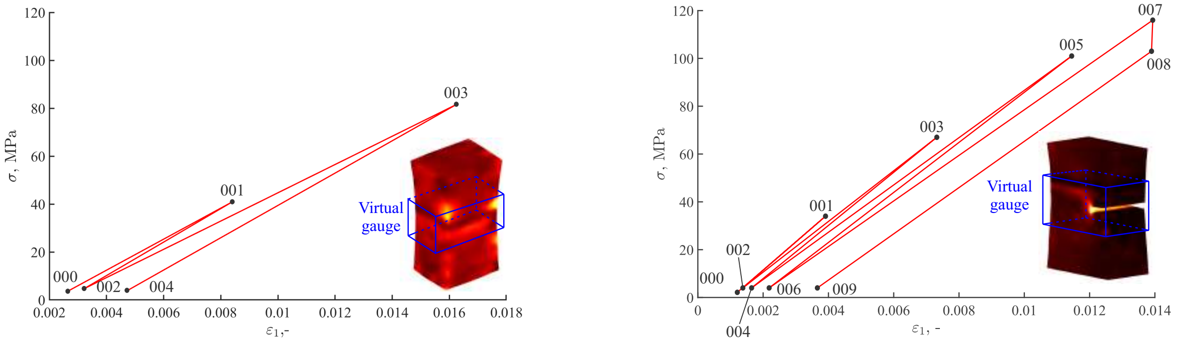

(a) **(b)**

Fig 4. Global material response of (a) the unnotched specimen and (b) the single notched specimen accounting for the mean major eigen strain ε_1 corresponding to the loading direction. The solid black circles depict the positions at which each new acquisition was performed. The blue boxes plotted over the major eigen strain fields of scan 003 for the unnotched specimen and scan 008 for the single notched specimen show the virtual gauges employed to calculate mean strain levels in the central part of the inspected ROIs.

Figure 4(b) displays the stress-strain response of the single notched specimen. From the reported stress-strain response, a decrease of macroscopic stiffness is observed. A mean major eigen strain level of 0.001 was reported for scan 000 acquired in the unloaded configuration. This offset stems from measurement uncertainties. At the peak of the first loading cycle (scan 001), a mean major eigen strain level of 0.004 was observed. Thus, the Young's modulus of the first loading cycle was estimated to be 10.6 GPa. Cycling the specimen up to 50% of its failure strength (scan 003) led to a mean major eigen strain of 0.0076, which resulted in a 2.8% decrease of the macroscopic stiffness. Upon the subsequent unloading (scan 004), the mean strain levels were very close to those observed for scans 000 and 002 (*i.e.*, no permanent strains at this stage). The subsequent loading cycle (between scans 004 and 005) led to a decrease of the macroscopic stiffness. In addition, permanent strains were observed after the specimen was unloaded, *i.e.*, a mean major eigen strain of 0.0024 was reported for scan 006. At the peak of the last loading cycle prior to specimen failure (scan 007), a mean major eigen strain of 0.0147 was reached leading to a Young's modulus of 9.1 GPa. The inspected specimen was held at that load level (F = 3710 N, σ = 116 MPa) to obtain an additional 3D image (continuous scan 008). As the stress level decreased to

$\sigma = 103$ MPa after acquiring scan 008, while the mean major eigen strain level remained approximately constant (the difference was within the range of measurement uncertainties), it was concluded that the investigated FRP composite exhibited stress-relaxation. As modest permanent strains ($\varepsilon_1 = 0.0039$) were observed after the last unloading cycle prior to specimen failure (scan 009), damage was expected to have occurred within the investigated material. The notched specimen failed at 135 MPa, *i.e.*, a level equal to that reported for the unnotched specimen. This result shows that the investigated material is notch-insensitive under the prescribed loading regime.

4.3. Major eigen strain and correlation residual fields

In the following section, the thresholded voxel-wise major eigen strain fields of both specimens are analyzed. The presented fields are complemented with the study of correlation residuals, which were thresholded in a way that all estimated levels that fell outside the specified range originated from mechanical causes (*i.e.*, the focus was put on the absolute range between 45 and 130 gray levels). Local increases in correlation residuals are attributed to the violation of the gray level conservation and displacement continuity associated with the tetrahedral mesh (*i.e.*, with damage initiation and growth). Last, the major eigen strain fields of both experiments were laid over the reference mesostructure in the background to investigate the effect of fiber yarn architecture on the strained band development.

4.3.1. Unnotched specimen

Figure 5(a) shows the initial major eigen strain field, while Figure 6(a) displays the initial correlation residual map of the unnotched specimen. In both fields, the fluctuations due to measurement uncertainties were hardly detectable within the selected range. For scan 001, one inner strained band extending through the whole ligament area was unveiled in the major eigen strain field, and already indicated the path to final failure (Fig. 5(b)). Additional strained areas emerged on the ligament edges due to specimen machining. The first localized phenomena were observed in the correlation residual map of scan 001 (marked with blue arrows in Fig. 6(b)). They correspond to the strained region detected in the major eigen strain field of the corresponding acquisition, thereby indicating the influence of specimen machining. The remainder of the correlation residual map exhibited sufficiently low values indicating successfully converged DVC analysis. Cracks were not observed within the region of the inner, horizontal strained band at this stage. A ring artifact appeared in the center of the specimen not only for scan 001, but for all subsequent acquisitions. The fact that the correlation residual maps unveiled the presence of this artifact proves that the registrations were successful (*i.e.,* initial differences between gray level volumes decreased to the noise level except where this phenomenon occurred). If the ring artifact had vanished, this would have meant that the algorithm tracked ring artifacts and not the underlying motion of the investigated material. The previously observed strained bands were still active upon specimen unloading (Fig. 5(c)). Yet, the majority of previously observed cracks near the specimen ligament edge were closed (Fig. 6(c)). Thus, damage deactivation and crack closure only occurred to a limited extent.

For scan 003, high strains developed within the bands on the ligament edges (Fig. 5(d)). These bands started propagating toward the material bulk. It is important to note that higher strain levels were observed within the bands occurring on the ligament edges than in the horizontal strained band, which was due to specimen machining. Numerous areas of higher correlation residuals unveiling the underlying mesostructure emerged in the material bulk near the specimen ligament edge (marked with blue and green arrows in Fig. 6(d)). Thus, a significant amount of damage growth set in. Yet, damage still did not initiate within the region of the horizontal strained band extending through the narrowest gauge section. Even though strain levels within the bands on the ligament edges were higher compared to that of the horizontal strained band, the latter still experienced an increase in strain levels compared to previous loading cycle. Therefore, the studied material could sustain high levels of damage (primarily induced by specimen machining) and still undergo an increase in strain levels within the horizontal strained band. During the last unloading prior to specimen failure, the strained bands were still active (Fig. 5(e)). Once again, partial crack closure took place (Fig. 6(e)). Still, cracks did not occur in the narrowest gauge section, even though the final failure path proceeded along the horizontal strained band.

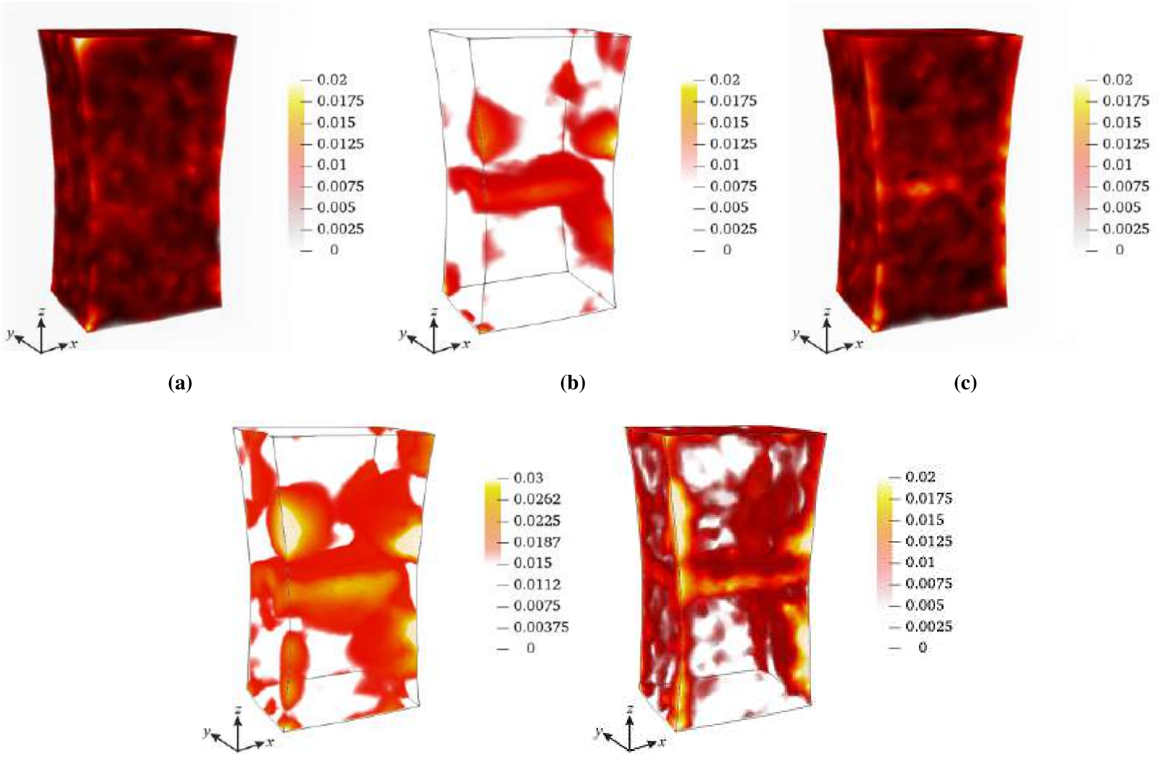

(a) (b) (c)

(d) (e)

Fig 5. Thresholded voxel-wise major eigen strain fields of the unnotched specimen calculated for scans (a) 000, (b) 001, (c) 002, (d) 003 and (e) 004.

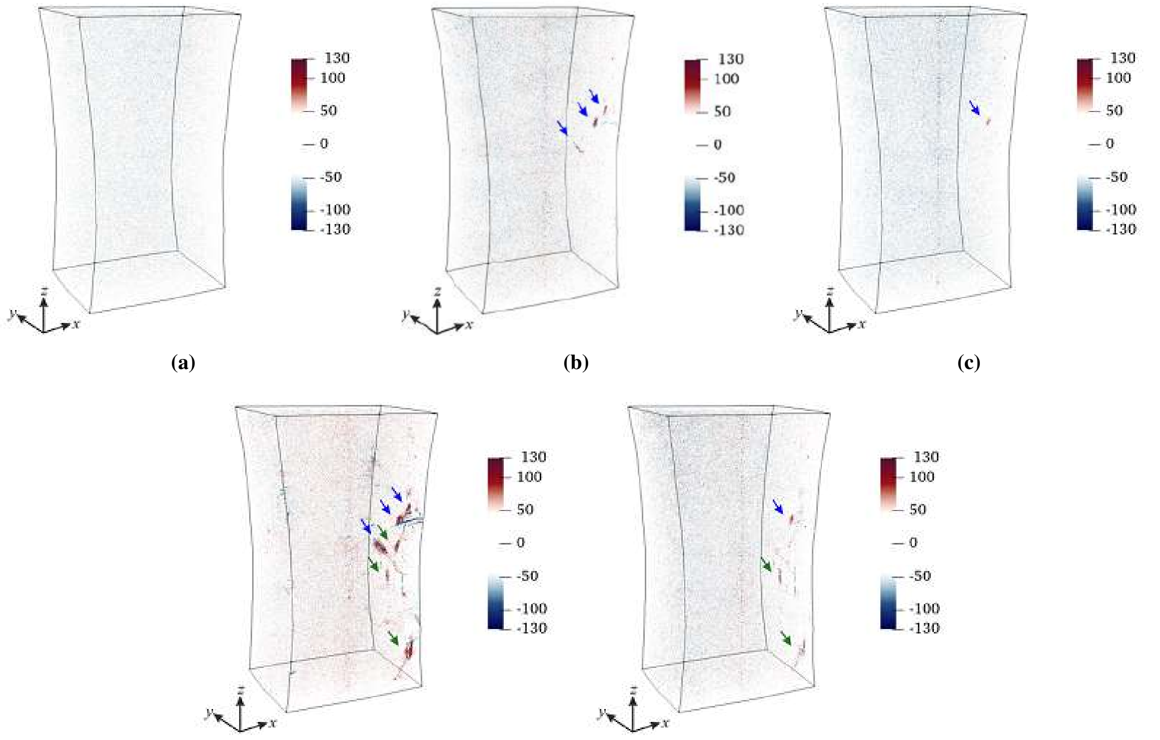

(a) (b) (c)

(d) (e)

Fig 6. Correlation residual maps of the unnotched specimen calculated for scans (a) 000, (b) 001, (c) 002, (d) 003 and (e) 004. The blue arrows depict the first detected damage, while the green arrows indicate additional damaged zones.

To further investigate the strained band activity, the RMS of major eigen strain fields per x, y and z slices (*i.e.*, plotted versus their x, y and z coordinates) were analyzed (Fig. 7). The plots show that, even after the first loading cycle (scan 001), permanent strains accumulated within the inspected ROI. Note that the dominant, horizontal strained band extending through the whole ligament area appeared at the beginning of the prescribed loading (scan 001). Yet, the strain levels gradually increased outside of the dominant strained band as the loading levels increased. For scan 004, the strain levels were higher than those of the previous unloaded states (scans 000 and 002), which leads to the conclusion that significant damage growth occurred during the *in-situ* cyclic experiment.

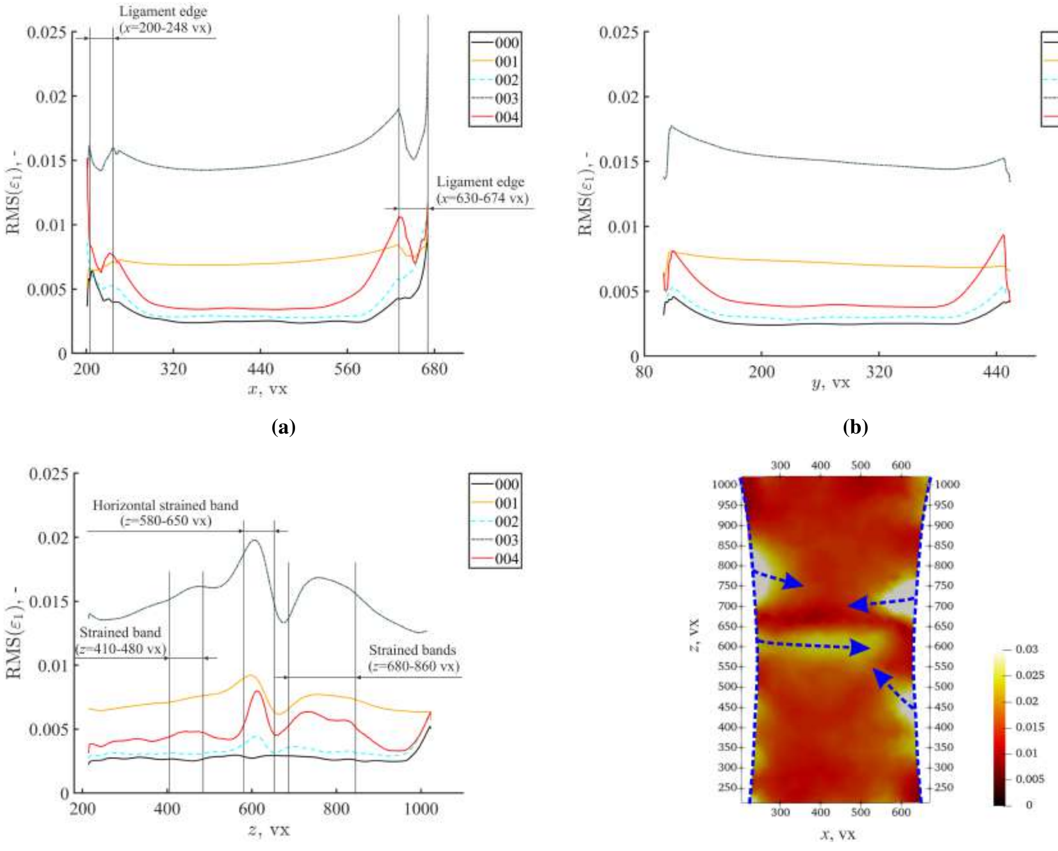

(a) (b) (c) (d)

Fig 7. Root mean square levels of major eigen strain fields plotted as functions of (a) x, (b) y and (c) z coordinates over the entire loading history. (d) The strained bands corresponding to the peaks of the RMS profiles are highlighted with blue dashed arrows on the front surface rendering of the major eigen strain field calculated for scan 003.

Plotting RMS(ε_1) versus their x coordinate (Fig. 7(a)) unveiled two peaks corresponding to elevated strains developing on the ligament edges. For scan 001, the strain levels within the bands inducing on the ligament edges were lower than those of the remaining part of the ROI. The main contribution to the increase in strain levels within the range $x = 248 - 630$ vx arose from the horizontal strained band (marked with a blue dashed arrow in Fig. 7(d)). For scan 002, higher permanent strains accumulated within the bands on the ligament edges compared to the remaining part of the ROI. Yet, for scan 003, the remaining part of the ROI (mainly the horizontal strained band) experienced an increase in strain levels, despite high strain gradients on the ligament edges. Subsequent specimen unloading once again revealed higher permanent strains accumulated on the ligament edges.

The analysis of RMS(ε_1) plotted versus their y coordinate (Fig. 7(b)) revealed the first peak corresponding to the front specimen surface (y = 105 vx). The reported increase arose from the strain field heterogeneities observed on the front specimen surface. The strain levels gradually decreased through the material bulk, whereas the second peak corresponds to the rear specimen surface ($y = 450$ vx). The main contribution to the latter was the horizontal strained band extending through the whole ligament area.

Last, RMS(ε_1) sections were analyzed with respect to their z-coordinate (Fig. 7(c)). The first peak was observed for $z = 410 - 480$ vx corresponding to the strained band on the ligament edge below the horizontal strained band (Fig. 7(d)). Next, significant growth of RMS(ε_1) was reported for $z = 580 - 650$ vx, which coincides with the horizontal strained band. The plotted RMS(ε_1) profiles again revealed that levels within the horizontal strained band increased, in spite of high strain gradients on the ligament edges. The final fracture path proceeded along the inner, horizontal strained band. The RMS(ε_1) profiles also revealed the third peak for $z = 410 - 480$ vx, which corresponds to the strained areas on the specimen ligament edges above the horizontal strained band (marked with blue dashed arrows in Fig. 7(d)). Consequently, the questions that arise are what could be the origin of the observed strained bands, and could the heterogeneities of the major eigen strain fields be linked with the heterogeneous mesostructure.

To study the effect of yarn architecture on the strained band development, thresholded voxel-wise major eigen strain fields of scan 003 (corresponding to the last loading cycle prior to specimen failure) were laid over the corresponding mesostructure sections in the reference configuration (HQ scan 0). The heterogeneities of the major eigen strain fields were analyzed for the front surface ($y = 105$ vx), mid-thickness section ($y = 280$ vx) and rear specimen surface ($y = 450$ vx), and shown in Figs. 8-10. The analyzed sections were also extracted from the *post-mortem* scan (HQ scan 1) to determine the crack morphology and correlate it with the strained band development.

First, the front surface was analyzed (Fig. 8(a)). The horizontal strained band propagated through the ligament area, and encompassed the fiber yarns being almost perpendicular to the loading axis (Fig. 8(c)). Additional strained areas appeared on ligament edges. The observed strain field heterogeneities outlined one part of the yarn architecture. The observed strained bands developed and propagated along the longitudinal axes of the fiber yarns inclined with respect to the loading axis. Conversely, the strained bands did not develop within regions of fiber yarns that were almost parallel to the prescribed loading. The *post-mortem* observations revealed that the final crack followed the early, horizontal strained band (marked with cyan dashed lines in Fig. 8(b)).

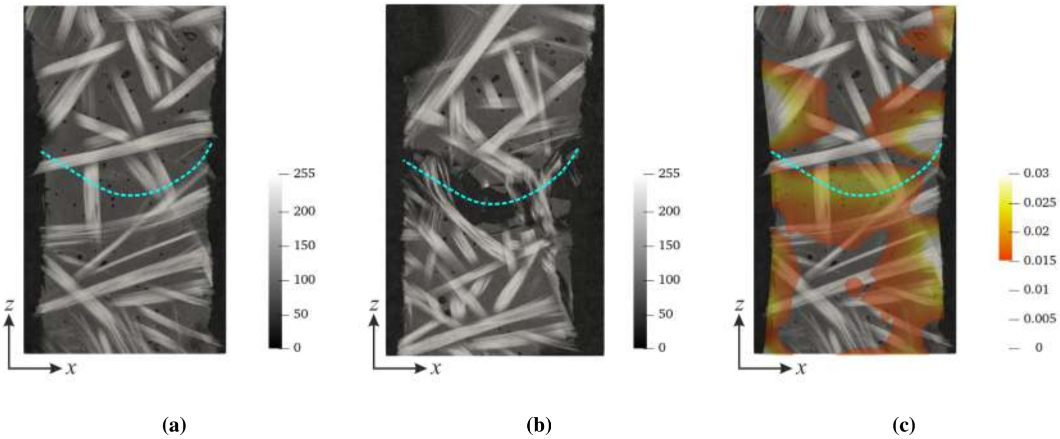

Fig 8. (a) Mesostructure section in the reference configuration (HQ scan 0) of the front specimen surface (y = 105 vx). (b) Corresponding section extracted from the *post-mortem* HQ scan 1. (c) Thresholded major eigen strains of scan 003 laid over the reference mesostructure. The cyan dashed lines denote the final failure path.

The same procedure was followed when considering the mid-thickness section (y = 280 vx), and is shown in Fig. 9. The dominant horizontal strained band enveloped the fiber yarns almost perpendicular to the loading direction. Additional strained bands appeared both above and below the horizontal strained bands. These areas encompassed the fiber yarns almost perpendicular to the loading direction. The final failure path followed the dominant, horizontal strained band. Yet, an additional crack branch appeared, which originated from the strained area on the ligament edge below the horizontal strained band.

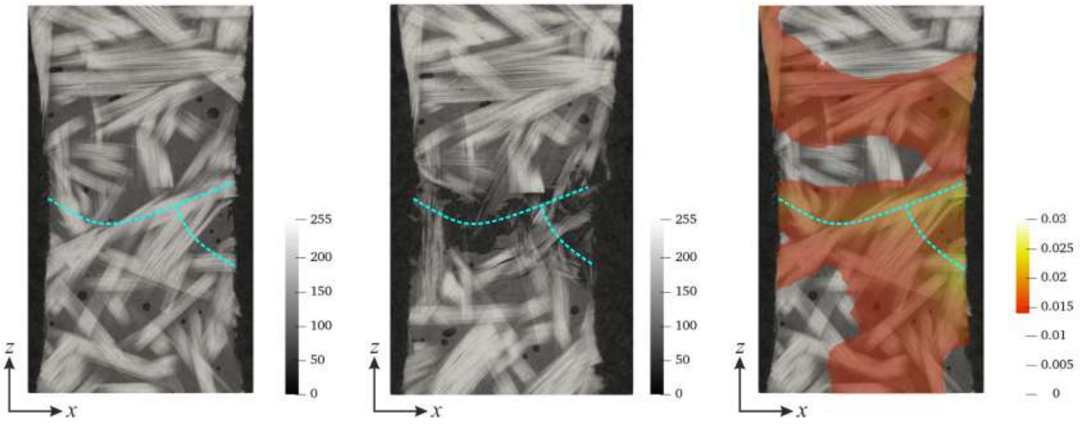

(a) (b) (c)

Fig 9. (a) Mesostructure section in the reference configuration (HQ scan 0) of the mid-thickness section (y = 280 vx). (b) Corresponding section extracted from the *post-mortem* HQ scan 1. (c) Thresholded major eigen strains of the mid-thickness section of scan 003 laid over the reference mesostructure. The cyan dashed lines depict the final failure path.

Last, the rear specimen surface (y = 450 vx, Fig. 10(a)) was analyzed. Once again, the strained bands outlined only one part of the yarn architecture, *i.e.*, they developed within the regions of fiber yarns perpendicular to the loading axis (Fig. 10(c)). The dominant, horizontal strained band propagated through the whole ligament area. The *post-mortem* analysis revealed that the final crack path followed this strained band (Fig. 10(b)). Thus, the phenomena observed for all three sections indicate that the strained band due to the yarn mesostructure prevailed over damage due to specimen machining.

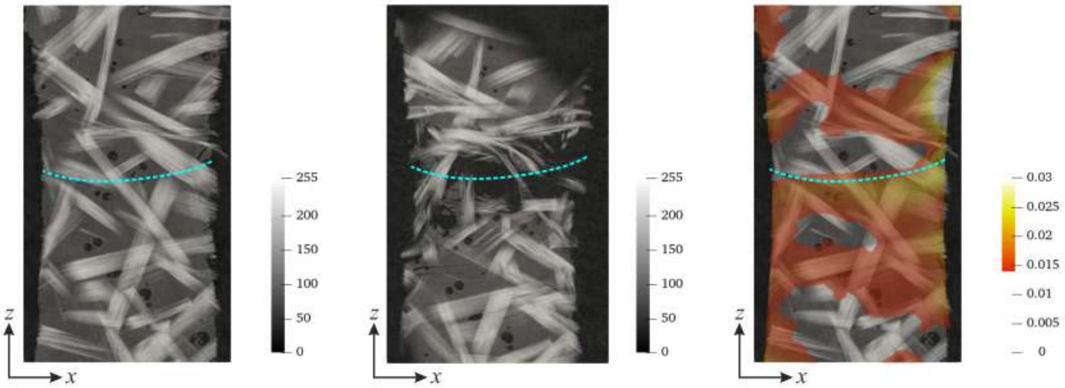

(a) (b) (c)

Fig 10. (a) Mesostructure section in the reference configuration (HQ scan 0) of the rear specimen surface (y = 450 vx). (b) Corresponding section extracted from the *post-mortem* HQ scan 1. (c) Thresholded major eigen strains of scan 003 laid over the reference mesostructure. The cyan dashed lines highlight the final failure path.

4.3.2. Single notched specimen

The thresholded voxel-wise major eigen strain fields and correlation residual maps of the single notched specimen are reported hereafter (Fig. 11 and Fig. 12). For scan 000, both fields exhibited fluctuations of small magnitude induced by measurement uncertainties (Fig. 11(a)). Upon cycling the specimen up to 25% of its failure strength (scan 001), high strain gradients were induced in the notched region (Fig. 11(b)). The formation of an inner, horizontal strained band originating from the notch root was unveiled. As in the case of the unnotched specimen, the observed strained band extended through the whole ligament area at the very beginning of loading, thereby already marking the future crack path. This phenomenon indicates the significant influence of material heterogeneities (*i.e.*, yarn mesostructure) on the final failure, even in the presence of a geometrical singularity inducing high strain concentration. It is also interesting to note that an additional strained band emanated from the notch root and extended below the notch toward the specimen bulk. Strain localization areas appeared on the ligament edges (both on the notch-free ligament edge and below the notch root), which indicated the influence of specimen machining (*i.e.*, thinning of the central part). A similar strain pattern was observed in the unnotched specimen. Furthermore, a ring artifact was observed in the correlation residual map of scan 001 (and for all the subsequent acquisitions), while the remainder of the ROI exhibited sufficiently low fluctuations ascribed to acquisition noise (Fig. 12(a)). This result indicated successfully converged correlations (the hypothesis of continuity of the displacement field was satisfied). Hence, damage growth did not yet occur, or if it had, it remained very low and at a scale lower than the scan resolution [28]. The subsequent unloading yielded homogeneous fields (Fig. 11(c) and Fig. 12(c)). The previously observed strained bands were no longer active, and the strain levels within the notched region decreased to that of scan 000.

The localization of elevated strains in the notched area was more apparent for scan 003 (Fig. 11(d)). As for the unnotched specimen, the strain levels within the horizontal strained band increased and the strained bands on the notch-free ligament. The latter broadened and started propagating toward the material bulk. In addition, the propagation of the strained band originating from the notch root and extending below it toward the notch-free ligament edge was even more pronounced. This strained band finally coalesced with those induced on the notch-free ligament edge. The first localized phenomena appeared in the correlation residual map of scan 003 (marked with blue arrows in Fig. 12(d)). Yet, they emerged near the notch-free ligament edge, and not in the notched area (as would be expected due to high strain activity in this region). This zone exemplifies the influence of specimen machining. The remainder of the ROI exhibited sufficiently low residuals proving that the kinematics of the investigated specimen was well captured. It is also meaningful to remember that the second loading step (between scans 002 and 003) resulted in the degradation of macroscopic stiffness (Fig. 4(b)), which indicates that cycling the specimen up to 50% of its failure strength induced damage inception and growth. Yet, localization of higher correlation residuals was not observed within the notched region. The notch-insensitivity of the investigated material was, therefore, demonstrated. Despite high strain gradients within the notched region, the investigated specimen experienced increases in strain levels within the observed strained bands determined by the underlying yarn mesostructure, and the first cracks induced by specimen machining appeared near the notch-free specimen ligament edge. Upon subsequent unloading, the major eigen strain field exhibited higher strain levels within the notched region and in the previously observed strained bands (Fig. 11(e)) compared to the corresponding fields of scans 000 (Fig. 11(a)) and 002 (Fig. 11(c)). Localized phenomena near the notch-free ligament edge observed in the correlation residual field of scan 003 disappeared (Fig. 12(e)). However, a permanent mean major eigen strain level of 0.0018 was reported at this stage (Fig. 4(b)). Consequently, it may be concluded that cycling the specimen up to 50% of its failure strength induced damage inception and growth, even though unloading resulted in damage deactivation.

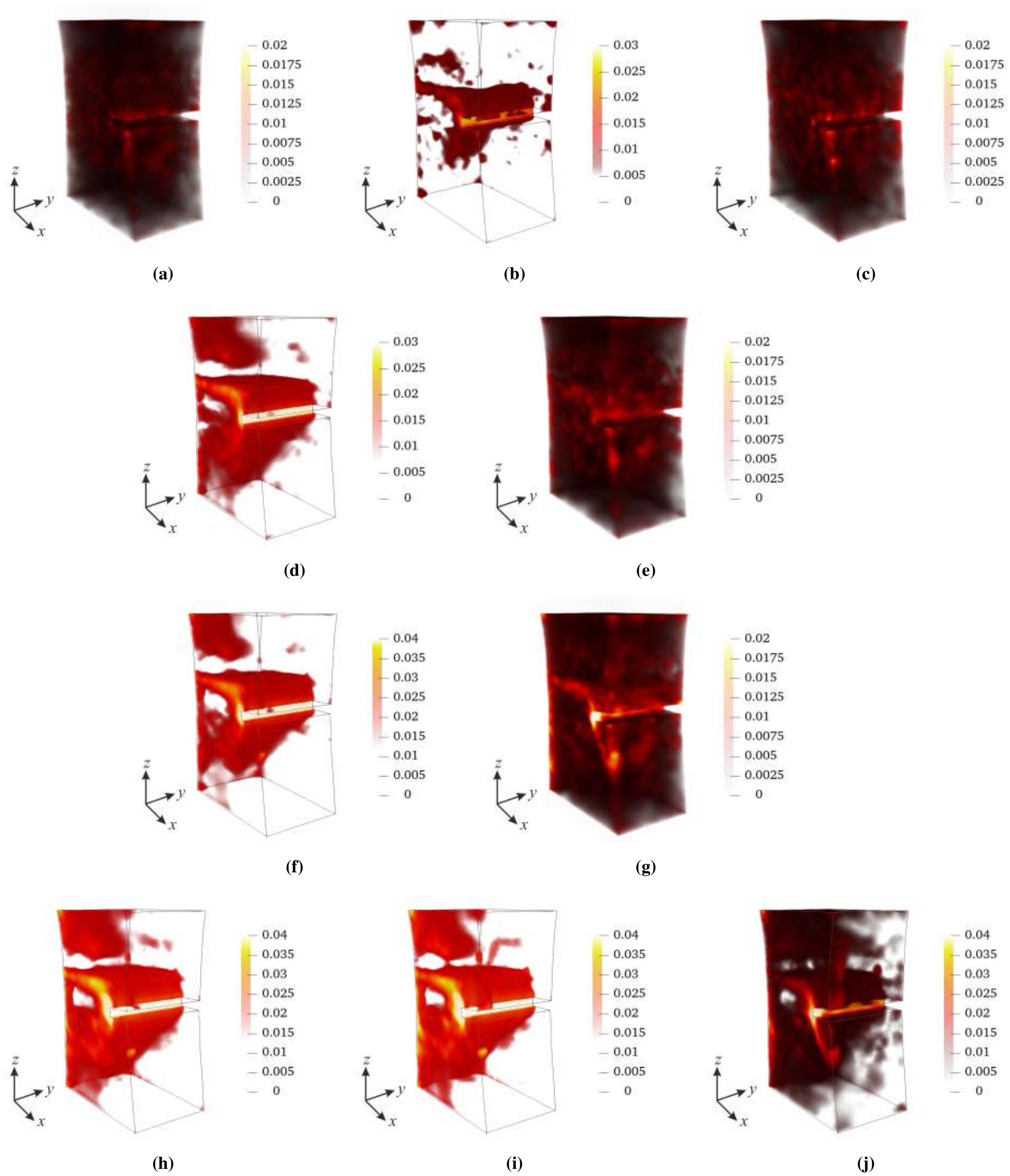

Fig 11. Thresholded voxel-wise major eigen strain fields of the single notched specimen calculated for scans (a) 000, (b) 001, (c) 002, (d) 003, (e) 004, (f) 005, (g) 006, (h) 007, (i) 008 and (j) 009.

At the peak of the third loading cycle (scan 005), strain levels within the previously observed bands increased in spite of high strains in the notched region (Fig. 11(f)). The strained area induced on the ligament edge below the notch root was more pronounced. The previously observed damaged zone near the notch-free ligament edge was once again apparent (Fig. 12(f)). Additional areas of elevated residuals appeared close to the notch-free ligament near the specimen front surface (y = 50 vx), as well as on the ligament edge below the notch root (marked with green arrows in Fig. 12(f)). The latter corresponds to the strained area on the ligament edge observed in the major eigen strain field of scan 005 (Fig. 11(f)). Furthermore, areas of elevated residuals emerged in the close vicinity of the notch root (marked with green arrows in Fig. 12(f)). It is important to outline that high strain gradients developed within the notched region at the very beginning of loading, before any signs of damage onset. They did not lead to premature fracture. Damaged zones were observed within the remainder of the ROI prior to damage initiation in the notched region. In addition, the final failure path followed the horizontal strained band. These observations once again highlighted the notch-insensitivity of the investigated material. For scan 006 acquired in the unloaded state, the previously observed strained bands were still active (Fig. 11(g)). Despite high strain gradients, areas of elevated residuals in the vicinity of the notch root vanished (Fig. 12(g)). Yet, damaged zones near the ligament edges remained active (marked with blue and green arrows in Fig. 12(g)). This trend once again exemplifies the notch-insensitivity of the studied material, namely, damage outside of the notched region was active and more pronounced even when the specimen was unloaded, in spite of high strain gradients induced in the notched area.

The strained band activity was even more apparent for scan 007 (Fig. 11(h)). Strain levels within the dominant, horizontal strained band increased, as well as in the strained areas on the ligament edges. The strained bands on the notch-free ligament fully merged with the band that emanated from the notch root and extended below it. In addition to the previously observed damaged areas, cycling the specimen to 90% of its failure strength induced the occurrence of multiple areas of elevated residuals within the inspected ROI (marked with red arrows in Fig. 12(h)). Cracks initiated within the whole notched region, in the material bulk above the notch, and on the notch-free ligament edge. Holding the specimen at the same load levels to acquire scan 008 led to an increase in strains within the observed strained bands (Fig. 11(i)). An additional strained band appeared from the notch root and started propagating below the notch reaching the previously observed strained area on the ligament edge. This phenomenon can also be observed in the corresponding residual map, *i.e.*, an additional region of elevated residuals propagating from the notch root emerged (Fig. 12(i)). Furthermore, the previously observed damaged regions became more dominant (Fig. 12(i)). The correlation residual maps of scans 007 and 008 showed that significant amount of damage growth occurred within the notched region. Yet, it did not lead to premature fracture, and additional areas of elevated residuals appeared within the material bulk (Fig. 12(i)). Upon subsequent unloading, the previously observed strained bands were still active (Fig. 11(j)). The corresponding major eigen strain field unveiled that the strained band originating from the notch root and propagating below it coalesced with the strained area on the ligament edge below the notch root. Moreover, some of the previously observed damage was deactivated (*i.e.*, partial crack closure occurred), as shown in Fig. 12(j). The damaged zones first observed when analyzing the correlation residual maps of scans 003 (Fig. 12(d)) and 005 (Fig. 12(f)) were still present, namely, the localization areas near the notch-free specimen ligament edge, on the ligament edge below the notch root and within the material bulk. Yet, the damaged zones within the notched region vanished, *i.e.*, damage deactivation and crack closure took place. Thus, damage outside of the notched region was still active and more pronounced even upon the last unloading cycle prior to specimen failure.

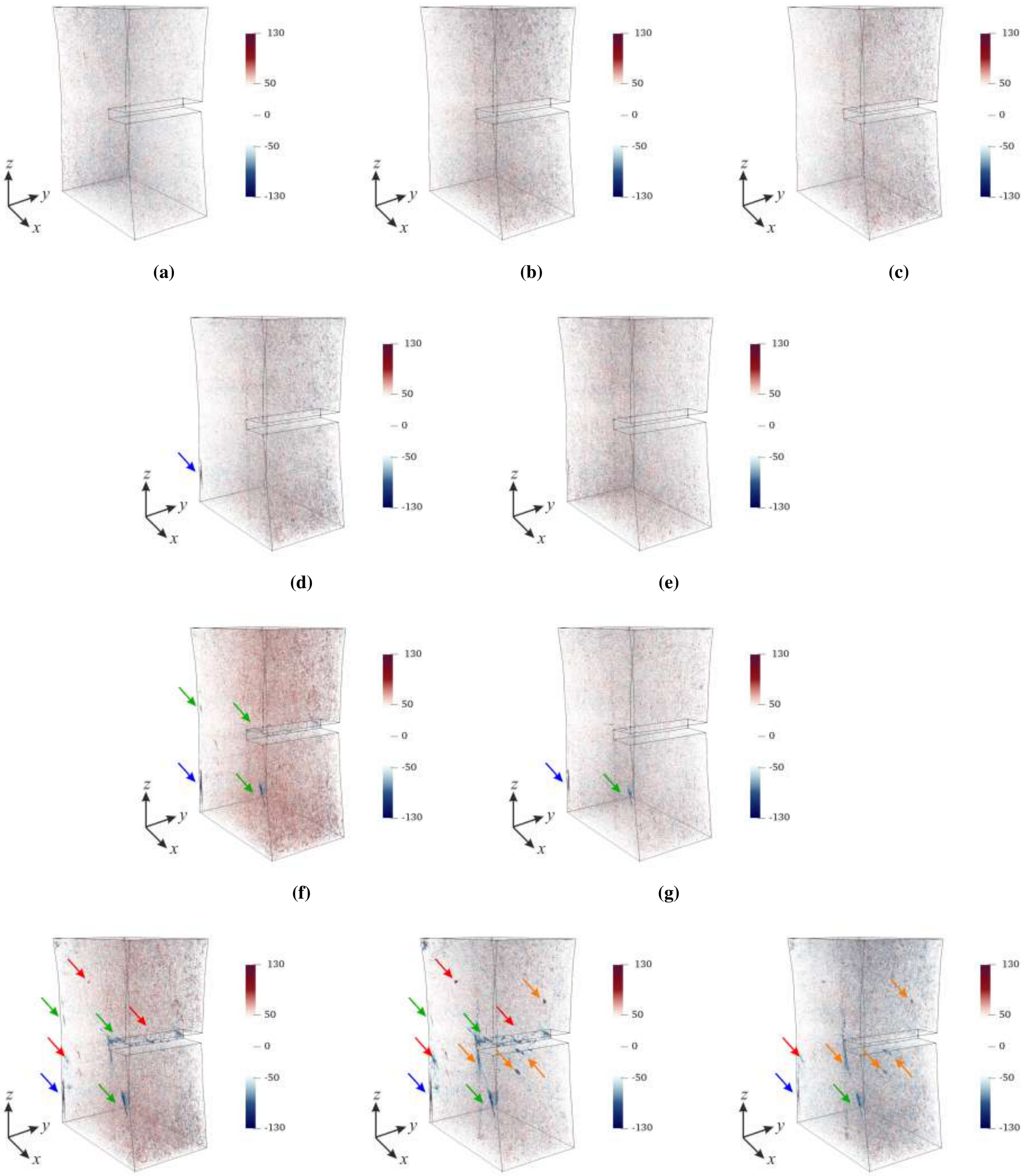

(a) (b) (c) (d) (e) (f) (g) (h) (i) (j)

Fig 12. Correlation residual maps of the single notched specimen calculated for scans (a) 000, (b) 001, (c) 002, (d) 003, (e) 004, (f) 005, (g) 006, (h) 007, (i) 008 and (j) 009. The blue arrows depict the first detected damage, while the green and red arrows indicate additional damaged zones. The orange arrows highlight cracks induced by holding the specimen at the reached load level to acquire additional scan 008.

Figure 13 shows RMS of major eigen strain fields per *x*, *y* and *z* slices for different scans acquired during the prescribed loading history. The plots show that cycling the specimen to 25% of its failure strength (scan 001) did not result in permanent strains as the RMS(ε_1) levels of scans 002 acquired after the specimen was unloaded remained close to those of the scan 000. Furthermore, RMS(ε_1) levels of scan 004 laid approximately in the range of scans 000 and 002, apart from differences in ligament edges, within the notched region and the strained band originating from the notch and propagating above the notch (*i.e.*, higher RMS(ε_1) levels of scan 004 were observed in the aforementioned regions compared to those of scans 000 and 002). Thus, low permanent strains were observed at this stage in the corresponding strained areas. As the load levels became higher, the major eigen strains within the ROI increased. The RMS(ε_1) levels of scan 009 were significantly higher compared to those of the previous unloaded stages. Hence, significant damage growth occurred during the *in-situ* cyclic experiment.

Plotting RMS(ε_1) levels versus their x coordinate (Fig. 13(a)) highlighted the first peak corresponding to elevated strains developing on the notch-free ligament edge ($x = 20 - 75$ vx), thereby indicating the impact of specimen machining. A gradual increase of RMS(ε_1) for all the acquired scans was observed for $x = 75 - 480$ vx, which was primarily attributed to the horizontal strained band emanating from the notch root (Fig. 13(d)). This band reached its peak at $x = 480$ vx corresponding to the notch root. The third interval of RMS(ε_1) increase occurred within the zone of $x = 590 - 645$ vx corresponding to the notched ligament edge. The main contribution to the reported increase arose from the strained band developing from the coalescence of the two strained areas; the first originating from the notch root, and the second developing on the ligament edge below the notch (Fig. 11). It is also important to note that higher RMS(ε_1) levels were observed on the notch-free ligament edges (Fig. 13(d)) for the scans acquired in the unloaded stages. The observed trends exemplify the damage tolerance of the material studied herein, namely, strained band activity outside the notched region prevailed in spite of high strain gradients induced by the geometric singularity (*i.e.*, notch).

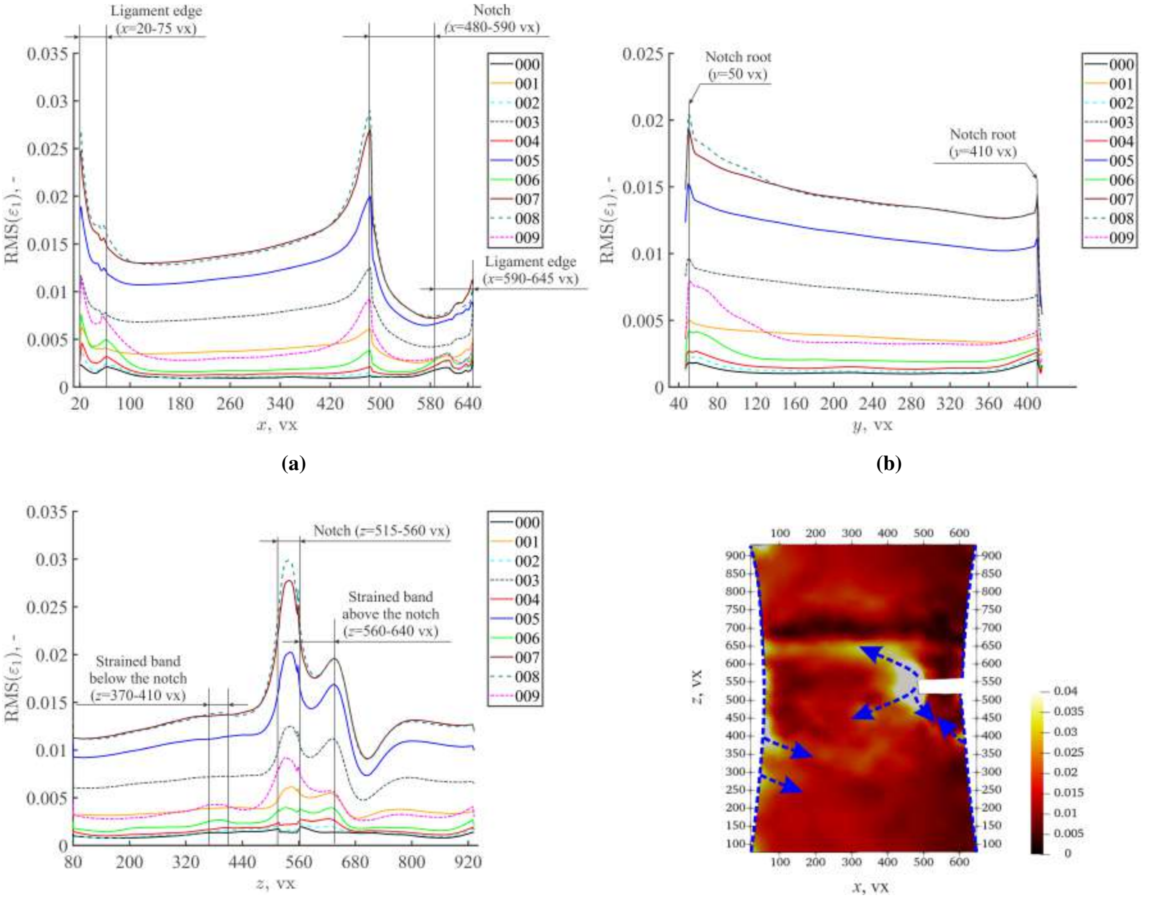

(a) (b)

(c) (d)

Fig 13. Root mean square levels of major eigen strain fields plotted as functions of (a) x, (b) y and (c) z coordinates over the entire loading history. (d) The strained bands corresponding to the peaks of the presented RMS profiles are highlighted with blue dashed lines (notch-free specimen ligament edge) and arrows (*i.e.*, strained bands emanating from the notch root and on the ligament edge below the notch) on the front surface rendering of the major eigen strain field calculated for scan 008.

The analysis of RMS(ε_1) levels plotted versus their y coordinate (Fig. 13(b)) shows that, despite high strains developing within the notched root, strain levels within the inspected ROI increased as the load levels became higher. The first peak coincides with the notch root on the front specimen surface (y = 50 vx). The strain levels gradually decreased when approaching the rear specimen surface (y = 410 vx), where RMS(ε_1) profiles reached their second peak. Last, RMS(ε_1) sections were also analyzed with respect to their z coordinate (Fig. 13(c)). The first peak was observed for z = 370 – 410 vx corresponding to the strained area developing on the ligament edge below the notch root (Fig. 13(d)). Next, significant growth of RMS(ε_1) levels was observed when $z = 515 - 560$ vx. The reported interval coincides with notch edges. The third increase of major eigen strains was observed within the region $z = 560 - 640$ vx (*i.e.*, the horizontal strained band emanating from the notch root, see Fig. 13(d)). The reported RMS(ε_1) profiles once again proved that high strains developed within the notched region. Yet, they did not lead to premature failure. The strained band activity in the remaining part of the ROI was pronounced, and strains gradually increased over the loading history, which led to the accumulation of permanent strains.

To study the effect of yarn architecture on the strained band development, thresholded voxel-wise major eigen strain fields of scan 008 were laid over the corresponding mesostructure sections in the reference configuration (HQ scan 0). The heterogeneities of the major eigen strain fields were analyzed for the front surface ($y = 50$ vx), mid-thickness section ($y = 233$ vx) and rear surface ($y = 450$ vx), and are shown in Figs. 14-16.

The major eigen strain field of the front specimen surface ($y = 50$ vx, Fig. 14(a)) was composed of multiple bands enveloping fiber yarns perpendicular to the loading direction (Fig. 14(c)). An additional strained band emanated from the notch root and started propagating below it reaching the strained area on the ligament edge. This phenomenon arose from the fact that the fiber yarn along which the strained band propagated was damaged (*i.e.*, debonding of individual fibers inside the yarn was observed in the reference configuration, see Fig. 14(b)). Thus, the major eigen strain field on the front specimen surface consisted of three dominant strained bands emanating from the notch root. The final crack propagated through the material bulk along the horizontal strained band (Fig. 14(b)). Yet, two additional crack branches appeared on the front specimen surface; the first one following the strained band reaching the notch-free ligament edge, and the second propagating below the notch toward the specimen ligament edge.

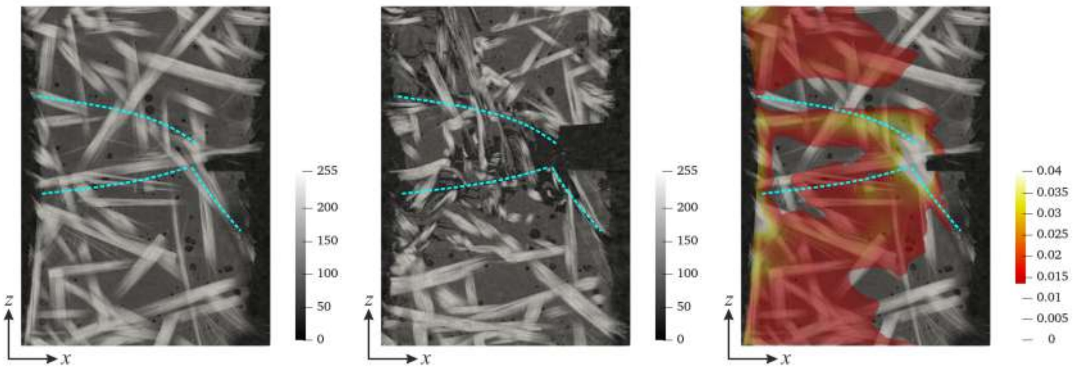

(a) (b) (c)

Fig 14. (a) Mesostructure section in the reference configuration (HQ scan 0) of the front specimen surface ($y = 50$ vx). (b) Corresponding section extracted from the *post-mortem* HQ scan 1. (c) Thresholded major eigen strains of scan 008 laid over the reference mesostructure. The cyan dashed lines denote the final failure path.

For the mid-thickness section ($y = 233$ vx, Fig. 15(a)), the horizontal strained band emanating from the notch root extended along the fiber yarns perpendicular to the loading axis (Fig. 15(c)). Outside of the horizontal strained band, elevated strains mainly encompassed fiber yarns inclined with respect to the loading axis, as opposed to the yarns being almost aligned with the loading direction. The effect of yarn misalignment is evidenced herein. The *post-mortem* observations revealed that the final failure path propagated along the dominant and horizontal strained band (Fig. 15(b)).

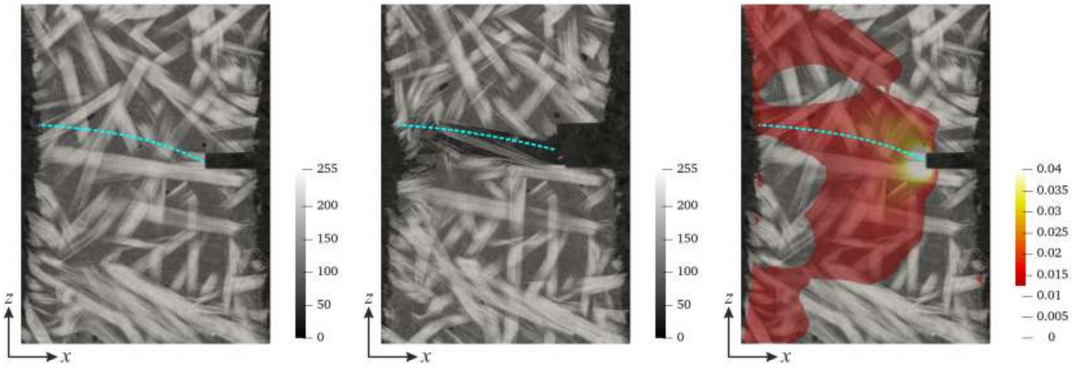

(a) (b) (c)

Fig 15. (a) Mesostructure in the reference configuration (HQ scan 0) of the mid-thickness section (y = 233 vx). (b) Corresponding section extracted from the *post-mortem* HQ scan 1. (c) Thresholded major eigen strains of scan 008 laid over the reference mesostructure. The cyan dashed lines denote the final failure path.

The same remarks apply for the rear surface (y = 410 vx, Fig. 16(a)). The major eigen strain field (Fig. 16(c)) exhibited two strained bands emanating from the notch root; the first one being the horizontal strained band, and the second propagating below the notch root reaching the notch-free ligament edge. The crack path followed the observed strained bands as shown in Fig. 16(b). The observed phenomena indicate that the final failure of the investigated material was pre-determined by the yarn mesostructure despite high strain gradients and damage growth within the material bulk. The strain activity induced by the fiber yarn architecture significantly contributed to the final failure, and thus reduced the notch-sensitivity of the investigated material.

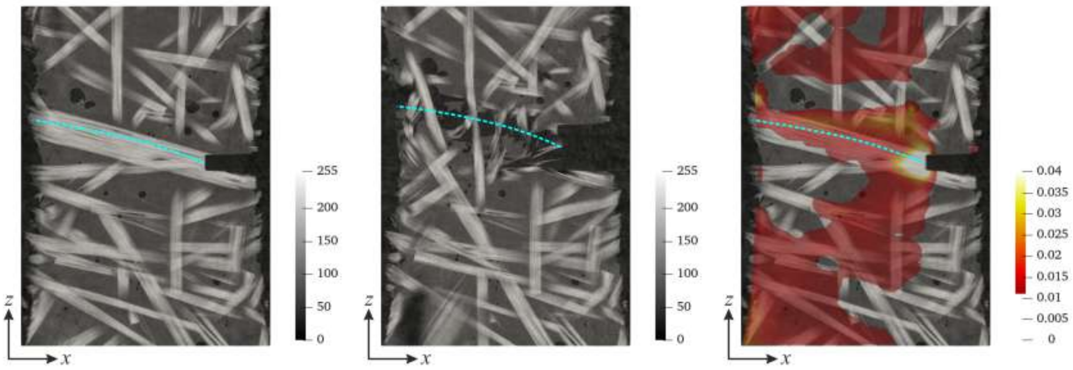

(a) **(b)** **(c)**

Fig 16. (a) Mesostructure section in the reference configuration (HQ scan 0) of the rear surface (y = 410 vx). (b) Corresponding section extracted from the HQ *post-mortem* scan 1. (c) Thresholded major eigen strains of scan 008 laid over the reference mesostructure. The cyan dashed lines denote the final failure path.

5. Conclusion

In the present work, two *in-situ* (tomography) experiments were performed on a continuous glass fiber mat reinforced polyester resin composite. The dogbone specimens were subjected to uniaxial cyclic tension. To induce higher strain gradients, a single rectangular notch was cut on the edge of one of the investigated specimens. The bulk kinematics was measured via FE-based DVC. The stress at failure of both specimens revealed that the investigated material was notch-insensitive. To further confirm this hypothesis, major eigen strains and correlation residual fields of both experiments were analyzed to study the strained band activity and damaged zones. Last, thresholded voxel-wise major eigen strain fields were laid over the corresponding mesostructure in the reference configuration to study the effect of yarn architecture on the strained band development. This work aimed at understanding the influence of the underlying yarn mesostructure on the strained band development and consequently the final failure of studied material.

The analysis of major eigen strain fields of both specimens revealed the formation of an inner, horizontal strained band extending through the whole ligament area even at the beginning of the loading history. Additional concentration zones appeared on the ligament edges of both specimens. The investigated material sustained an increase in strain levels within the horizontal strained band, in spite of high strain gradients on the ligament edges and, in the case of the single notched specimen, in the notch root. Furthermore, it was shown that the strained bands developed before any signs of damage onset within both specimens, which was significantly influenced by the underlying material heterogeneities (*i.e.*, the observed strained bands enveloped and propagated along the fiber yarns significantly inclined to the loading direction). It is important to note that the final crack path of both specimens proceeded along the early horizontal strained band extending through the whole ligament area. This phenomenon indicates that the strained band effect determined by the yarn mesostructure prevailed over damage due to machining and/or the presence of the geometric singularity (*i.e.*, notch). The final failure of the investigated material was, therefore, pre-determined by the yarn mesostructure despite high strain gradients and damage growth within the material bulk. The present study documents new sets of experimental evidence of strained band development and failure of investigated material. It was shown that the latter was primarily driven by the heterogeneous yarn mesostructure.

The experimental results presented herein clarified the origin of the strained bands, and thus provided a better understanding of strain localization and failure of the investigated polymer matrix composite. The ability of FE-DVC to provide measurements even in the presence of strained bands and highly localized damage was highlighted. The same protocol may be utilized to explore strain and damage interactions for different loading conditions typical of engineering applications. Besides the reported specimen geometries, other shapes and scales may be studied, in particular, specimens with initial higher or lower strain concentrations or singularities.

CRediT author statement

Ana Vrgoč: Software, Formal analysis, Writing - Original Draft, Visualization
Zvonimir Tomičević: Conceptualization, Validation, Resources, Writing - Review and

Editing, Supervision, Project administration

Benjamin Smaniotto: Investigation

François Hild: Software, Validation, Writing - Review and Editing, Supervision

Compliance with Ethical Standards

The authors have no conflict of interest to declare.

Acknowledgments

This work was performed within the FULLINSPECT project supported by the Croatian Science Foundation (UIP-2019-04-5460 Grant). It was also partially supported by the French "Agence Nationale de la Recherche" through the "Investissements d'avenir" program (ANR10-EQPX-37 MATMECA Grant).

References

[1] Khechai A, Tati A, Guerira B, Guettala A, Mohite PM. Strength degradation and stress analysis of composite plates with circular, square and rectangular notches using digital image correlation. Composite Structures 2018;185:699–715.

[2] Prashanth S, Km S, Nithin K, Sachhidan . Fiber reinforced composites - a review. Journal of Material Sciences and Engineering 2017;6:1–6.

[3] Nguyen VD, Wu L, Noels L. A micro-mechanical model of reinforced polymer failure with length scale effects and predictive capabilities. validation on carbon fiber reinforced high-crosslinked rtm6 epoxy resin. Mechanics of Materials 2019;133:193–213.

[4] Green B, Wisnom MR, Hallett SR. An experimental investigation into the tensile strength scaling of notched composites. Composites Part A-applied Science and Manufacturing 2007;38:867–78.

[5] Xu MX, Huang J, Zeng B, He D, Fu Y, Deng HL. Effect of notch on static and fatigue properties of t800 fabric reinforced composites. Science and Engineering of Composite Materials 2020;27:335 –45.

[6] Grédiac M, Hild F, editors. Full-Field Measurements and Identification in Solid Mechanics. London (UK): ISTE / Wiley; 2012.

[7] Buljac A, Jailin C, Mendoza A, Neggers J, Taillandier-Thomas T, Bouterf A, et al. Digital volume correlation: Review of progress and challenges. Experimental Mechanics 2018;58:661–708.

[8] Sutton M. Computer vision-based, noncontacting deformation measurements in mechanics: A generational transformation. Applied Mechanics Review 2013;65(AMR-13-1009):050802.

[9] Tomičević Z, Roux S, Hild F. Evaluation of fatigue crack network growth in cast iron for different biaxial loading paths via full-field measurements. International Journal of Fatigue 2016;92:281–303.

[10] Zaplatić A, Tomičević Z, Čakmak D, Hild F. Improvement of the arcan setup for the investigation of thin sheet behavior under shear loading. Experimental Mechanics 2022;62:313–32.

[11] Tomičević Z, Bouterf A, Surma R, Hild F. Damage observation in glass fiber reinforced composites via μ-tomography. Materials Today: Proceedings 2019;12:185–91.

[12] Brault R, Germaneau A, Dupré J, Doumalin P, Mistou S, Fazzini M. In-situ analysis of laminated composite materials by x-ray micro-computed tomography and digital volume correlation. Experimental Mechanics 2013;53:1143–51.

[13] Croom B, Jin H, Mills BE, Carroll J, Long K, Brown JA, et al. Damage mechanisms

in elastomeric foam composites: Multiscale x-ray computed tomography and finite element analyses. Composites Science and Technology 2019;169:195–202.

[14] Wang K, Pei S, Li Y, Li J, Zeng D, Su X, et al. In-situ 3d fracture propagation of short carbon fiber reinforced polymer composites. Composites Science and Technology 2019;182:107788.

[15] Sutton M, Wolters W, Peters WH, Ranson W, McNeill S. Determination of displacements using an improved digital correlation method. Image and Vision Computing 1983;1:133–9.

[16] Chu T, Ranson W, Sutton M, Peters W. Applications of digital-image-correlation techniques to experimental mechanics. Experimental Mechanics 1985;3(25):232–44.

[17] Réthoré J, Tinnes J, Roux S, Buffière J, Hild F. Extended three-dimensional digital image correlation (X3D-DIC). C R Mécanique 2008;336:643–9.

[18] Roux S, Hild F, Viot P, Bernard D. Three dimensional image correlation from X-Ray computed tomography of solid foam. Composites Part A: Applied Science and Manufacturing 2008;39(8):1253–65.

[19] Vrgoč A, Tomičević Z, Smaniotto B, Hild F. Application of different imaging techniques for the characterization of damage in fiber reinforced polymer. Composites Part A: Applied Science and Manufacturing 2021;150.

[20] Buljac A, Navas VMT, Shakoor M, Bouterf A, Neggers J, Bernacki M, et al. On the calibration of elastoplastic parameters at the microscale via x-ray microtomography and digital volume correlation for the simulation of ductile damage. European Journal of Mechanics A-solids 2018;72:287–97.

[21] Hild F, Roux S. Comparison of local and global approaches to digital image correlation. Experimental Mechanics 2012;52:1503–19.

[22] Tomičević Z, Hild F, Roux S. Mechanics-aided digital image correlation. The Journal of Strain Analysis for Engineering Design 2013;48:330 –43.

[23] Mendoza A, Neggers J, Hild F, Roux S. Complete mechanical regularization applied to digital image and volume correlation. Computer Methods in Applied Mechanics and Engineering 2019;355:27–43.

[24] Vrgoč A, Tomičević Z, Zaplatić A, Hild F. Damage analysis in glass fibre reinforced epoxy resin via digital image correlation. Transactions of FAMENA 2021;45(2):1–12.

[25] Buljac A, Helfen L, Hild F, Morgeneyer T. Effect of void arrangement on ductile damage mechanisms in nodular graphite cast iron: In situ 3d measurements. Engineering Fracture Mechanics 2018;192:242–61.

[26] Kak A, Slaney M. Principles of computerized tomographic imaging. New York: IEEE Press; 1988.

[27] Leclerc H, Neggers J, Mathieu F, Hild F, Roux S. Correli 3.0. 2015. doi:`IDDN.FR.001.520008.000.S.P.2015.000.31500`.

[28] Hallo G, Lacombe C, Parreault R, Roquin N, Donval T, Lamaignère L, et al. Subpixel detection of laser-induced damage and its growth on fused silica optics using registration residuals. Optics express 2021;29 22:35820–36.